Available online at www.sciencedirect.com
SCIENCE DIRECT®
International Journal of Solids and Structures 42 (2005) 2911–2928
INTERNATIONAL JOURNAL OF SOLIDS and STRUCTURES
www.elsevier.com/locate/ijsolstr

Acoustic damping characterization and microstructure evolution in nickel-based superalloy during creep

Toshihiro Ohtani [a,*], Hirotsugu Ogi [b], Masahiko Hirao [b]

[a] *Materials Lab., Ebara Research Co. LTD., 4-2-1 Hon-Fujisawa, Fujisawa, Kanagawa 251-8502, Japan*
[b] *Graduate School, Osaka University, 1-3 Machikaneyama-Cho, Toyonaka, Osaka, 560-8531, Japan*

Received 2 March 2004; received in revised form 24 September 2004
Available online 6 November 2004

Abstract

We studied the microstructure evolution of a nickel-based superalloy, Waspaloy, subjected to tensile creep at 1073 K through monitoring of shear-wave attenuation and velocity using electromagnetic acoustic resonance (EMAR). Contactless transduction based on the Lorentz force mechanism is the key to establishing a monitor for microstructural change in the bulk of the metals with a high sensitivity. There is a clear relationship between the attenuation and the life fraction. In the interval, 35 to 40% of the creep life, attenuation experiences a peak, being independent of the applied stress. This novel phenomenon is interpreted in terms of drastic change in dislocation mobility and the coarsening of γ'-precipitates, which is supported by SEM and TEM observations. At this period, dense dislocations start tangling to γ'-precipitates and the coarsening and condensation of γ'-precipitates become saturated. The EMAR has a potential to assess the damage advance and to predict the remaining creep life of metals.

Keywords: Electromagnetic acoustic resonance; Nickel-based super-alloy; Creep damage; Internal friction; Dislocation

1. Introduction

A large percentage of fossil power plants were constructed during 1960's and 70's and have been used beyond the design life of 30 to 40 years while they have undergone progressive damage caused by creep (e.g., Viswanathan, 1989). By shifting the base load of power from fossil power plants to nuclear power plants, they are faced to even more severe operating condition such as daily or weekly startup and shutdown in order to correspond to rapid change of the demand for power. Furthermore, the steam pressure

* Corresponding author. Tel.: +81 466837625; fax: +81 466837635.
E-mail address: ohtani.toshihiro@er.ebara.com (T. Ohtani).

0020-7683/$ - see front matter © 2004 Elsevier Ltd. All rights reserved.
doi:10.1016/j.ijsolstr.2004.09.037

and temperature in boiler components are increasing to improve the thermal efficiency for energy saving and reduction of CO_2 emission. This percentage is likely to become more significant during next decade because new plants could not be constructed due to economical and environmental issues. Therefore, a high emphasis is being placed on the economic and technical justifications for continued operation for the aging plants (e.g., Dooley and Viswanathan, 1987). As the consequence of this trend, material's degradation is being accelerated.

To safely operate their plants, a life prediction technology with a nondestructive or analytical method is needed to evaluate the present state of their materials and to assess the remaining life of them. The analytical methods (e.g., Kachanov, 1958; Rabotnov, 1969; Dunn et al., 1985; Ellis et al., 1987; Miller, 1987; Bhandari et al., 2000; Bergheau et al., 2004) estimate the remaining life based on the operating history, component geometry, and material property (Viswanathan, 1989). Although uncertainties of these parameters, as well as in calculational methods used, lead in erroneousness of the outcomes, the analytical procedures are a necessary first step for identifying potential damage sites and damaging transients. Without such an analysis, isolated problems could be found by nondestructive examination, but it would de difficult to identify the root caused of the problems. For the life prediction, it is essential to use nondestructive and analytical methods together.

To date, a replication method has been widely used (e.g., Neubauer and Wedel, 1983; Delong, 1987; Viswanathan, 1989) in nondestructive evaluation. This method provides an approach to microstructural evaluation in localized surface regions. It, however, gives no information regarding volumetric damages like creep damage proceeded inside of a material, not from the surface (Jaske et al., 1983). It performs under empirical decisions by well skilled operators and is time- and labor-intensive. It is important the technique should provide simple and quick measurement to cope with the large number of measuring points. There were a number of candidates to detect the damage. Ultrasonic methods have a unique of evaluating the internal damage state with comparatively simple and easy instrumentation, while many others including x-ray, replication, hardness-based and magnetic-properties-based methods; merely inspect the surface or near-surface region of the materials.

The ultrasonics have been studied for estimating the creep damage (e.g., Willems et al., 1987; Ledbetter et al., 1987; Nakashiro et al., 1987; Kishimoto et al., 1988; Birring et al., 1989; Hirao et al., 1990; Morishita and Hirao, 1997). In these applications, the ultrasonic attenuation and velocity have been measured with contacting piezoelectric transducer.In some case, the velocity decreased with damage accumulation; in other, this tendency was not observed. The velocity was often more sensitive to the damage than the ultrasonic attenuation.The creep mechanism is dominated by dislocations, which also dissipate acoustic energy causing ultrasonic attenuation (or internal friction). It is believed, however, that attenuation changes measured using conventional transducers cannot precisely reflect the creep damage because the so measured attenuation includes not only the attenuation of the sample, but also the damping through the transducers, the couplant and the buffer, the reflection and transmission losses at the interface, and the energy leakage into the transducer. Because the attenuation within the sample has to be considered to evaluate the creep damage, these extra losses are much greater than the attenuation within the sample (Goebbels, 1980) and must be removed with the proper correction procedure (Papadakis, 1984). But it is difficult in practice because the contacting conditions such as coupling pressure and the thickness of the couplant, which are required for the correction, can easily vary during the deformation or damage processes. The viscous couplant and the higher pressure required for the transduction of the shear wave make the coupling state more changeable.

In recent years, the electromagnetic acoustic resonance (EMAR) (Hirao et al., 1993; Hirao and Ogi, 1997) has been applied to the nondestructive inspection and determination for materials characterization (e.g., Johnson et al., 1992, 1994; Clark et al., 1992; Hirao et al., 1993). The EMAR is a combination of the resonant technique and a non-contacting electromagnetic acoustic transducer (EMAT) (Hirao et al., 1993; Hirao and Ogi, 1997). Generally, the transduction efficiency of an EMAT is considerably lower than

that of the piezoelectric transducer. But, this shortcoming can be overcome by incorporating it in the resonant method, in which the highly and coherently overlapping echoes construct easily detectable signal amplitude, although a single echo is still weak. Furthermore, this technique can evaluate the absolute value of ultrasonic attenuation of the metals. The EMAR is the ideal method for sensing the material's microstructural change as the creep progresses via ultrasonic, especially ultrasonic attenuation. There have been only a few studies, which intend to assess the creep damage with this technique (e.g., Ohtani et al., 2001a,b).

This study proposes to use the EMAR to make non-contact measurement of ultrasonic attenuation and velocity during creep tests. A Nickel-based super-alloy (WASPALOY), commonly used for disk material of aircrafts and power-plant turbines, was used for the sample. A bulk-wave EMAT (Hirao and Ogi, 1997) was used in order to measure the ultrasonic attenuation and velocity in the thickness direction of a specimen as the creep progresses. There is a good correlation between the attenuation coefficient and the life fraction estimated by the modified θ projection (Maruyama et al., 1985) and the rupture parameter, P (Maruyama and Oikawa, 1987). The attenuation coefficient shows a maximum around 35 to 40% of creep life, being independent of the applied stress. The change of the attenuation coefficient corresponded to the evolution of the dislocation structure, especially the change of dislocation mobility and the coarsening of γ'-precipitates. The relationship between the attenuation coefficient and the dislocation structure can be explained by the string model of dislocation vibration (Granato and Lücke, 1956). EMAR will assess the creep damage and predict the remaining life of metals.

2. Experiments

2.1. Materials

The material was from a hot-rolled commercial plate of a Nickel-based super-alloy (WASPALOY), of which the high temperature strength and creep resistance are enhanced by γ' precipitates and carbides, mainly of the type of $M_{23}C_6$ (e.g., Rosen et al., 1993). The heat treatment is as follows; solution at 1313 K for 1 h and water quenching, stabilization at 1118 K for 4 h and air cooling and aging at 1033 K for 16 h and air cooling. Specimens for the creep test were machined as shown in Fig. 1; the gauge section has 5 mm thick, 18 mm wide and 35 mm long. The rolling direction was parallel to the longitudinal direction of the specimen. The chemical composition and mechanical properties at room temperature and 1073 K were shown in Tables 1 and 2, respectively.

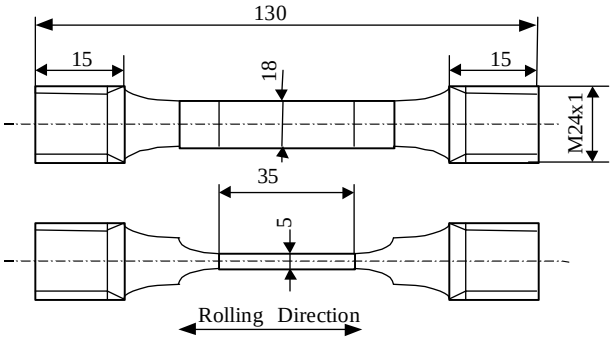

Fig. 1. Geometry and dimension of creep specimens in millimeters.

Table 1
Chemical composition of Waspaloy [wt%]

C	Si	Mn	P	S	Cu	Ni	Cr	Mo	Ti	Al	Fe	Co	Zr	B
0.07	0.04	0.01	0.004	0.001	0.02	BAL	19.59	4.14	2.92	1.33	0.58	13.17	0.05	0.004

Table 2
Mechanical properties of Waspaloy at the room temperature and 1073 K

Temp	0.2% proof stress (MPa)	Ultimate tensile strength (MPa)	Elongation (%)
RT	996	1400	22.3
1073 K	689	772	22.4

2.2. EMAT

We used a shear-wave EMAT of $10 \times 10\,mm^2$ active area, which consists of an elongated-spiral coil and a pair of permanent magnets in opposite directions being normal to the specimen surface as shown in Fig. 2. The shear wave is induced by the following mechanism. When an rf burst current is supplied to the coil placed close to a conducting material, eddy currents are generated in the surface of the material. These currents interact with the static magnetic field produced by a pair of permanent magnets and generate the Lorentz force upon electrons carrying the eddy currents. This force gives rise to the mechanical body force and generates a shearing vibration through the collision with ions or other transformation mechanism. As shown in Fig. 2, the Lorentz force is principally parallel to the surface and results in the polarized shear wave propagating in the thickness direction of the sample. The receiving principle is based on the reverse process of the generation.

2.3. Measurement of attenuation with EMAR

We measured resonant frequencies and attenuation coefficients for resonant modes with the superheterodyne spectrometer (Furtonko et al., 1992). We have several steps to measure the pure attenuation

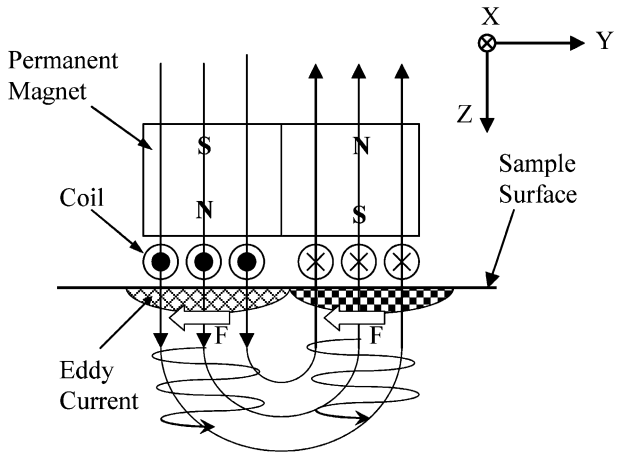

Fig. 2. Operation of the shear-wave EMAT. Lorentz force, F, excites the shear wave propagation in the Z direction.

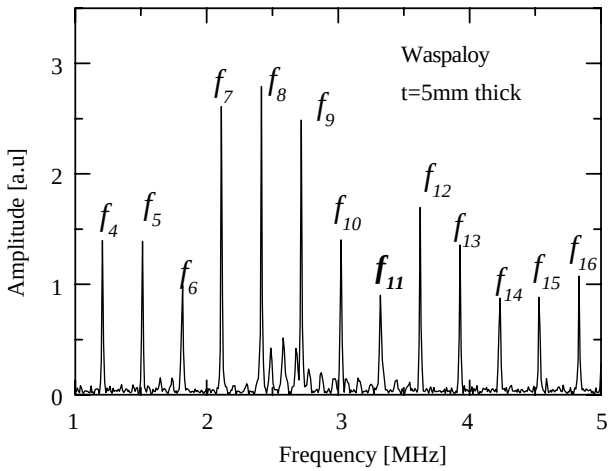

Fig. 3. Measured resonant spectrum for Waspaloy plate of 5-mm thickness by EMAR.

within the material, which are independent of measurement conditions including the EMAT used, the sample thickness, the surface condition, the liftoff, and the operator (Ogi et al., 1995). First, a resonant spectrum is obtained by sweeping the frequency of the rf burst. Shown in Fig. 3 is typical resonant spectrum for Waspaloy plate of 5 mm thickness. Resonant modes appear at an equal interval and are determined by the following equation; $f_N = NC/(2d)$, where N is the resonant mode, C the wavespeed, d the thickness of the sample, f_N the N-th resonant frequency. Second, the resonant frequency is determined from the center axial of the Loretzian function fit to the spectrum around the peak. Third, we measured the ringdown curve by driving the EMAT at the resonant frequency. Fig. 4 shows the measured ringdown curve at the eleventh mode (f_{11}) shown in Fig. 3. Finally, the attenuation coefficient is obtained by fitting an exponential decay to the ringdown curve and extracting the time constant.

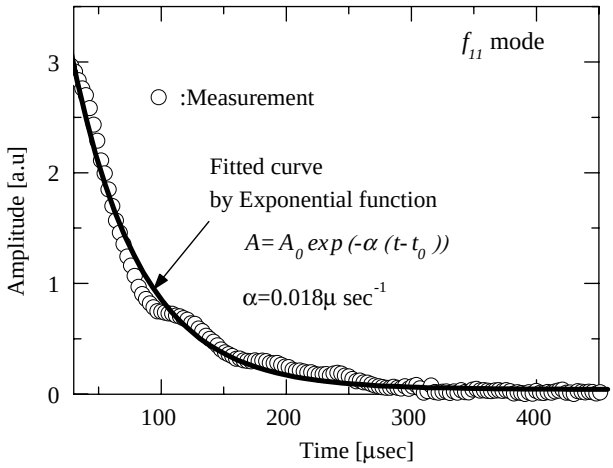

Fig. 4. Measured ringdown curve of the eleventh resonant mode in Fig. 3 and the fitting to an exponential decay.

2.4. Creep tests

Creep tests were carried out at 1073 K in air for three stresses of 140, 150 and 160 MPa with lever-type equipments. Two different creep tests were conducted. They are referred to as *Interrupted* and *Continuous tests*. In *Interrupted test*, we interrupted creep loading and furnace-cooled the samples. After measuring ultrasonic properties (the attenuation coefficients and velocity), we restarted the creep test. We repeated this procedure for every 30 or 100 h until the rupture. In *Continuous test*, twelve specimens were prepared for 140 MPa. The creep test was carried out until the creep strain reached a target value. After the creep test, ultrasonic properties were measured. A series of crept samples with different strains was obtained. Alongside the samples, we attached the unstressed samples to investigate only the effect of thermal history.

To further study the microstructure evolution as the creep progress, we observed the microstructures of specimens in continuous test with optical microscope (OM), scanning electron microscope (SEM) and transmission electron microscope (TEM). TEM foils were sliced from the mid-plane at the specimen's center using oil-cooling electro-discharge wire to 0.3 mm thick and then carefully polished with SiC paper to 0.2mm thick. Electrolytic polishing in 10% phosphoric acid-ethanol solution induced small center holes. Transmission electron microscopy operating at 250 kV was used to obtain the micrographs at thinnest parts around holes. These micrographs are taken in the computer with the scanner for further analysis.

Interrupted test is similar to the measurement in the field because of continuously monitoring the damage evolutions of the same sample, while *Continuous test* is conducted in order to investigate the relationship between the microstructure evolution and the change of ultrasonic properties as the creep progress.

3. Results

3.1. Interrupted test

We measured the resonant frequencies for 1 to 6 MHz range and their attenuations during the creep test of Waspaloy with bulk-wave EMAT. Fig. 5 displays the frequency dependence of the attenuation coefficient, α ; in *Interrupted test* (1073 K, 140 MPa). The rupture life, t_r, is 1024.5 h. The polarization of the shear

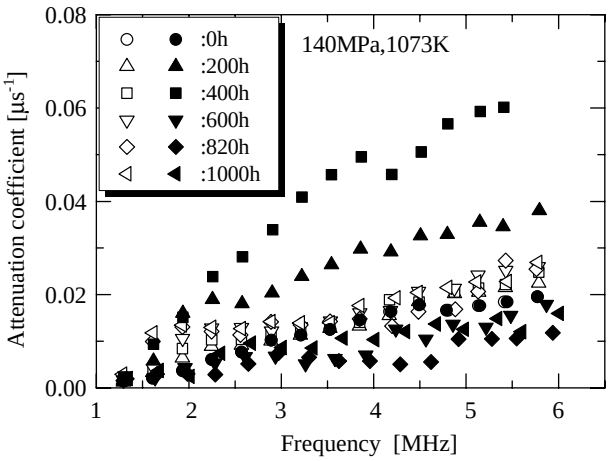

Fig. 5. The frequency dependence of the attenuation coefficient, α, in *Interrupted test* (1073 K, 140 MPa). Solid marks are the data of the reference sample and the open marks are for crept sample. The rupture life is 1024.5 h.

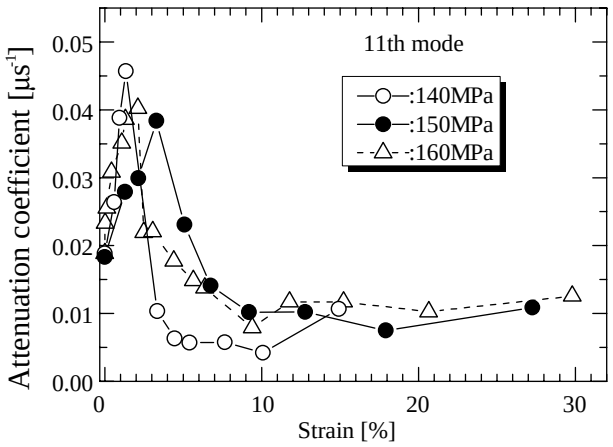

Fig. 6. The relationship between the creep strain and the attenuation coefficients for 160, 150 and 140 MPa at the 11th resonant mode in *Interrupted test*. The rupture lives are 480.9 h for 160 MPa, 518.9 h for 150 MPa and 1024.5 h for 140 MPa.

wave is parallel to the load. We observe that α always increases with resonant frequency. After increasing from the start to 400 h, α decreases in the course of creep. Only the heat treatment little affected α.

In Fig. 6, we plot the creep strain versus the attenuation coefficients for three applied stresses (160, 150 and 140 MPa) at the 11th resonant mode (around 3.5 MHz). Rupture lives are 480.9 h for 160 MPa, 518.9 h for 150 MPa and 1024.5 h for 140 MPa. αs rapidly increase with increasing strain. After showing a maximum value at the strain of 2 to 3%, they quickly decrease to the creep strain of 5 to 7 %. Afterwards, they remain nearly unchanged to rupture. Similar behavior is observed under other resonant modes. The maximum value of attenuation is two times larger than the attenuation before the creep.

Shown in Fig. 7 is the relationship between α, velocity change, $\Delta V/V_0$ (V_0:initial velocity), creep strain, and the life fraction, t/t_r (the creeping time/the rupture life), at the 11th resonant mode under 140 MPa. α initially increases as the creep progress and shows a maximum value around at $t/t_r = 0.4$. After that, α returns to the gradual trends of increase with time, whereas $\Delta V/V_0$ gradually increases until $t/t_r = 0.4$, slightly decreases until $t/t_r = 0.8$, and then decreases to the rupture. The maximum decrement of $\Delta V/V_0$ was about 0.5%. Because the evolution of α and $\Delta V/V_0$ are not monotonous, it is advisable to use both properties to evaluate the creep damage. Similar behavior is observed under other resonant modes and stresses.

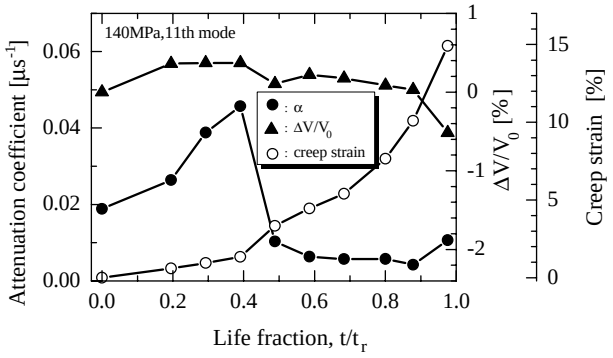

Fig. 7. The relationship between α, $\Delta V/V_0$, creep strain, and the life fraction, t/t_r, at the 11th resonant mode under 140 MPa in *Interrupted test*.

3.2. Continuous test

We prepared twelve specimens with different creep strains. In Fig. 8, creep curves in *Continuous test* are shown, of which specimens reached target strains at 140 MPa. It can be seen that each specimen shows different creep curve, in spite of same test condition. As a reference, the creep curve of a ruptured specimen is shown.Shown in Fig. 9 is the relationship between the creep strain reached and creeping time. Each point is corresponding to each specimen. The experimental values are very scattered. This figure does not show a good correlation between the creep stain and the time. That is, even though the creeping time becomes longer, the degree of creep strain does not become larger. In other word, the time cannot be a reference of creep damage.

Shown in Fig. 10 is the relationship between the creep strain and the attenuation coefficients at three resonant modes (the fifth, eighth, eleventh). α rapidly increases with increasing strain. After showing peaks

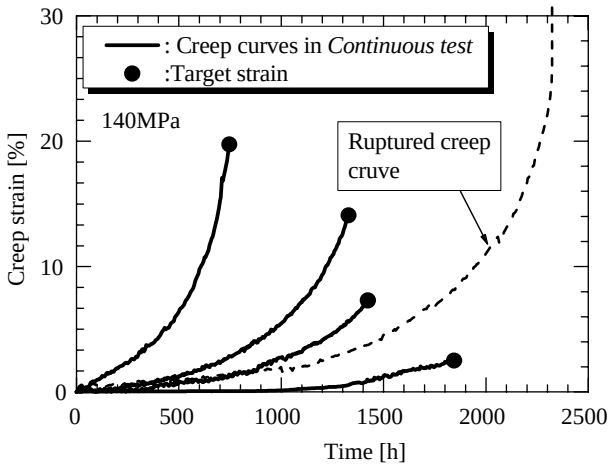

Fig. 8. The creep curves in *Continuous test* (140 MPa, 1073 K).

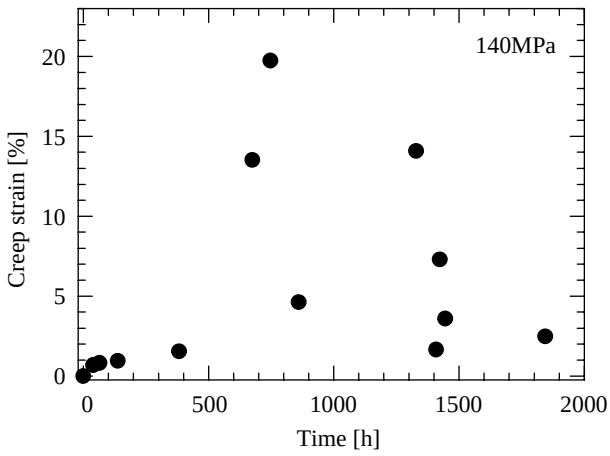

Fig. 9. The creep strains reached versus times in *Continuous test* (140 MPa, 1073 K).

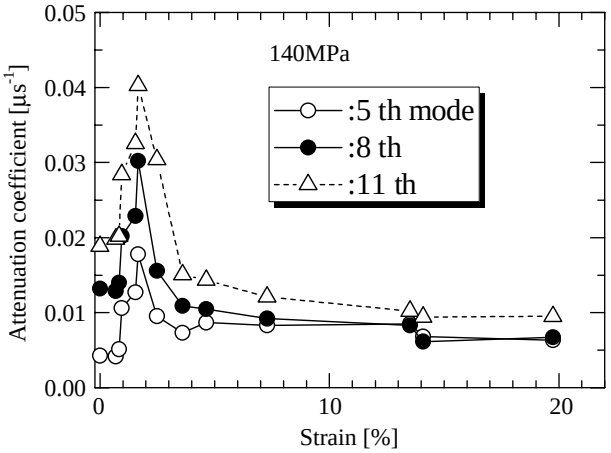

Fig. 10. The relationship between creep strains versus the attenuation coefficients at the 5th, 8th, 11th resonant modes in *Continuous test*. The polarization is parallel to the stress direction.

at the strain of 2%, it quickly decreases until 4% of the creep strain. Afterwards, it remains nearly unchanged. The trend is very similar in *Interrupted test*.

As shown in Fig. 9, the creep rupture strain and time are inapplicable to the remaining life prediction. To estimate the rupture life and the life fraction of each specimen, the modified θ projection (Maruyama et al., 1985) and a rupture parameter, P (Maruyama and Oikawa, 1987) are applied, which describe as follows:

$$\varepsilon = \varepsilon_0 + A\{1 - \exp(-\beta t)\} + B\{\exp(-\beta t) - 1\} \tag{1}$$

$$P = (1/\beta)\ln\{(\varepsilon_r - \varepsilon_0 - A)/B\} \tag{2}$$

$$t_r = CP^q, \tag{3}$$

where ε_0, A, B, β are all determined parameters by a nonlinear regression to measured creep curve, which are function of stress and temperature, ε_r the strain to rupture, t_r rupture life, and C, P constants. Eq. (1) may be seen as the summation of a primary creep component, which saturates with time and a tertiary creep component, which accelerates exponentially with time.

Steps for the estimation were as follows:

(1) Rupture tests of several specimens were conducted in order to obtain data of creep strain-time from the start to the rupture under several different stresses.
(2) Parameters: ε_0, A, B, β in Eq. (1) were determined from the nonlinear regression to the data.
(3) The rupture parameter, P was calculated by substituting these parameters for Eq. (2). ε_r was set at 25%.
(4) Constants: C, q in Eq. (3) were determined from the rupture lives.
(5) Parameters: ε_0, A, B, β, P, of each specimen were determined as stated above first 3 steps.
(6) The estimated rupture life, t_r, of each specimen was calculated by substituting P for Eq. (3).
(7) The creeping time, t, was divided to lead t/t_r.

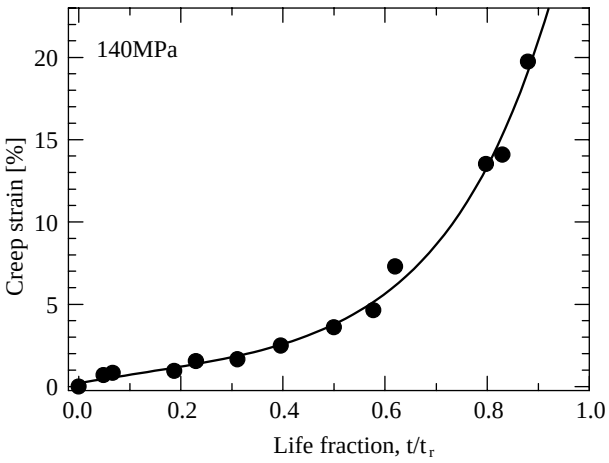

Fig. 11. The creep strain reached versus estimated life fraction in *Continuous test* (140 MPa, 1073 K).

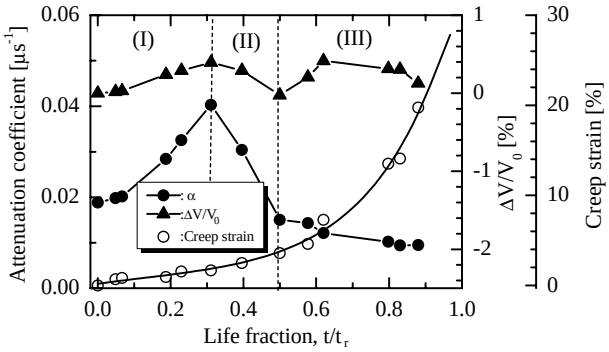

Fig. 12. The relationship between α, $\Delta V/V_0$, creep strain, and t/t_r, at the 11th resonant mode under 140 MPa in *Continuous test*.

The resultant relation between t/t_r-creep strain is shown in Fig. 11, where is expressed with one line. These data show a good correlation between t/t_r and the creep strain. Fig. 12 displays the relationships between α, $\Delta V/V_0$, creep strain, and t/t_r, at the 11th resonant mode. The trend is very similar in *Interrupted test* : that α increases, shows a peak at $t/t_r = 0.3$, and decrease until the failure and the velocity also showed the similar evolution as in Fig. 7. Similar behavior is observed under other resonant modes. Therefore, by the observing microstructures of specimens in *Continuous test*, we could find what influences the attenuation evolution as the creep progress.

4. Discussion

Possible factors contributing to the change in the attenuation coefficient are the scatterings at grain boundaries, precipitates and voids, and dislocation damping in a MHz frequency range (Truell et al., 1969; Goebbels, 1980). We discuss their influence on the attenuation coefficient independently to identify a dominant factor.

4.1. Grain scattering

We observed the change of the average grain size as the creep progress with the optical micrographs. Fig. 13 shows optical micrographs of the crept sample at $t/t_r = 0$ and 0.6. The stress direction is parallel to the longitudinal direction. Precipitates in grains and on grain boundaries are observed before the creep (Fig. 13(a)), whereas they seem to vanish on the grain boundaries at $t/t_r = 0.6$ (Fig. 13(b)). Micrographs were taken into the computer with the scanner, and the average grain size was calculated. As shown in Fig. 14, the average grain size remains nearly unchanged as the creep progress. When the grains are much smaller than ultrasonic wavelength (>0.5 mm), the attenuation caused by scattering is given by (Truell et al., 1969; Goebbels, 1980).

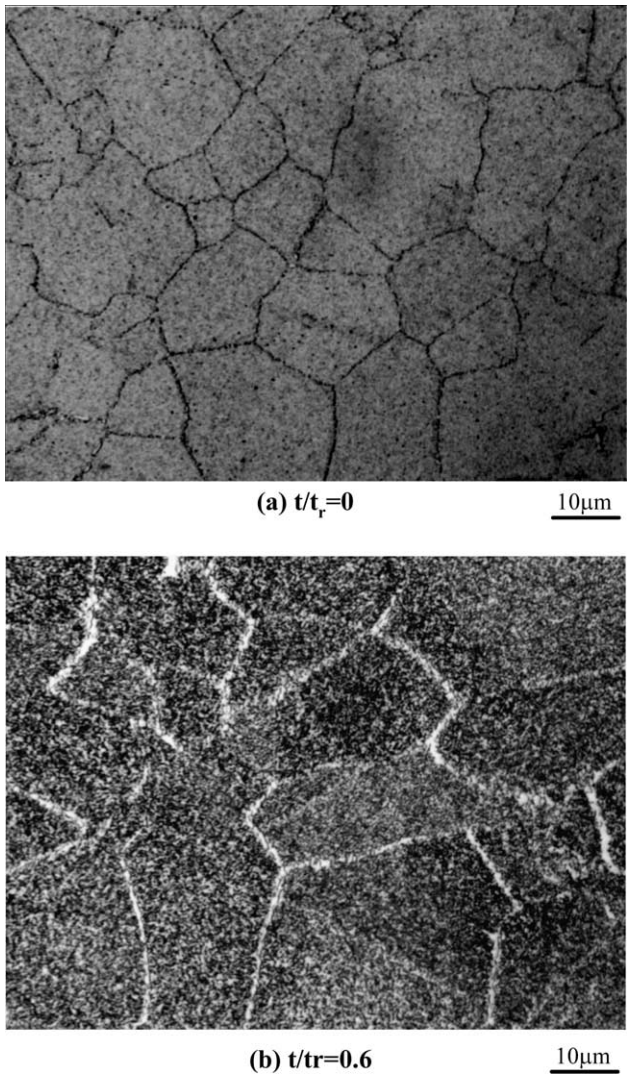

Fig. 13. Optical micrograph of a crept specimen at $t/t_r = 0$, 0.6 in *Continuous test* (140 MPa, 1073 K).

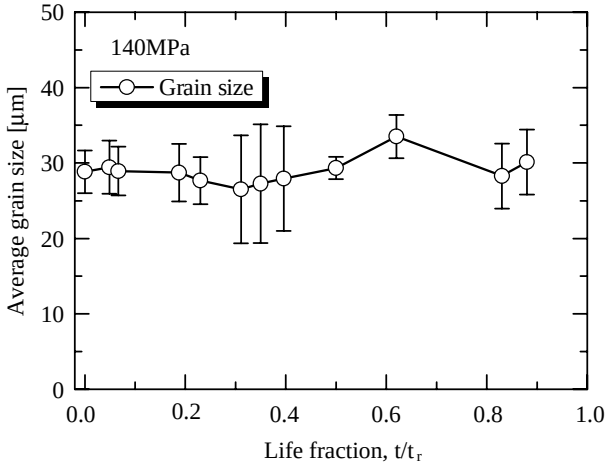

Fig. 14. Change of the average grain size as creep progress in *Continuous test* (140 MPa, 1073 K).

$$\alpha_s = Sd^3f^4, \tag{4}$$

where S denotes the scattering factor, d the average grain size, and f frequency. Thus, nearly constant grain size as shown in Fig. 14 can not explain the change of attenuation coefficients like in Fig. 12.

4.2. Scattering from precipitates

Shown in Fig. 15 are the SEM micrographs of the crept samples at $t/t_r = 0$ and 0.5. Precipitates are observed in grains and on the grain boundaries before the creep. From the EDX measurement (Arrow in Fig. 15), spherical precipitates in grains identified to be γ'-precipitates, the intermetallic compound composed of Al, Ti and Ni; and precipitates on grain boundaries to be Chromium-Carbide. Their average sizes of γ'-precipitate and the Cr-carbide before the creep test are 0.05 μm and 1 μm, respectively. Fig. 15(b) shows that the size of γ'-precipitate and the distance between them are much larger than those in Fig. 15(a) and then the γ'-precipitates near grain boundaries disappear. White bands near grain boundaries appear as shown in Fig. 13(b). Shown in Fig. 16 are the evolutions of the average diameter and the number density of γ'-precipitates during the creep. From the start to about 30% of life time, the diameter increases and the density decreases rapidly. Since then, they levels off. Because the sizes (>2 μm) were much smaller than the probing wavelength (>0.5 mm), the scattering in the Rayleigh region does occur (Goebbels, 1980),

$$\alpha_s = \frac{n_0\delta}{2} \sim C_0a^2(ka^4), (ka \ll 1), \tag{5}$$

where n_0 denotes the volume density of the scatter, δ is the scattering cross section, k the wave number and a the radius of the scatterer. C_0 is constant depending on the wave mode and the scatterer's type (i.e. inclusion). From Eq. (5), we calculated α_s to be less than 1% of measured value. This effect causes only negligible change in α. On the assumption that the attenuation increases in a monotonous way from SEM micrographs and Fig. 16, the change of α as shown in Fig. 12 fails to explain. Therefore, the dislocation damping can solely explain the observed acoustic response.

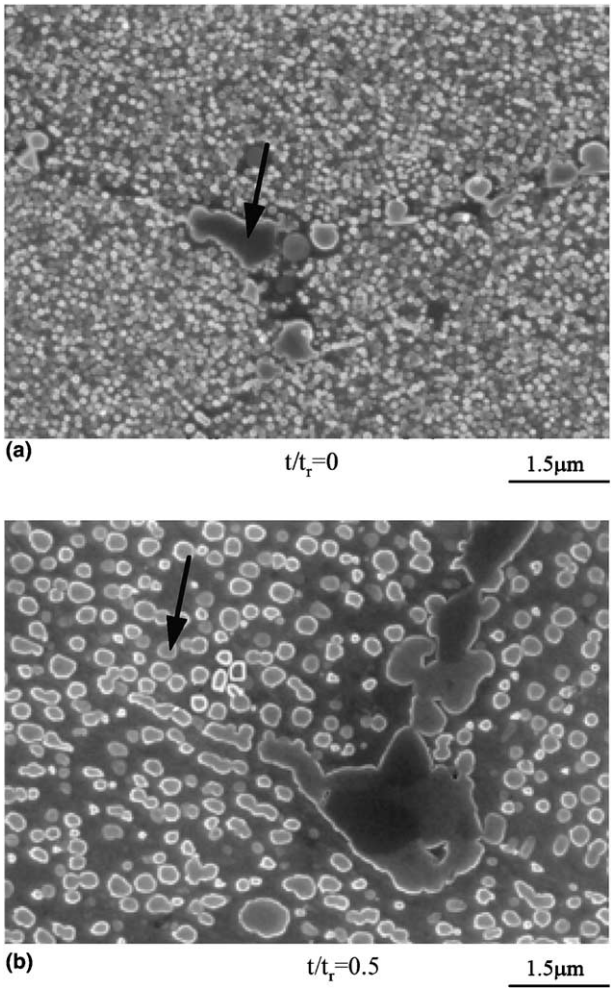

Fig. 15. Scanning electron micrographs of crept specimens at $t/t_r = 0$, 0.5 in *Continuous test* (140 MPa, 1073 K).

4.3. Dislocation damping

Dislocations vibrate responding to the ultrasonic stress with a phase lag because of viscosity and absorb of the energy. This anelastic mechanism also lowers the ultrasonic velocities. Dislocation lines are pinned by point defects, precipitates and other dislocations. These pinning points act as nodes of the vibration of elastic strings. According to Granato and Lücke (1956) string model, damping and velocity change due to dislocations for the lower frequencies take the form;

$$\alpha = A_1 \Lambda L^4 f^2 \quad \text{and} \quad \frac{\Delta V}{V} = A_2 \Lambda \, L^2, \tag{6}$$

where A_1 and A_2 are positive constants depending on the shear modulus, Poisson's ratio, specific damping constant, and Burger's vector. Λ is the dislocation density and L the dislocation length. Thus, α is proportional to Λ and the fourth power of L of the effective dislocations, which can vibrate responding to the

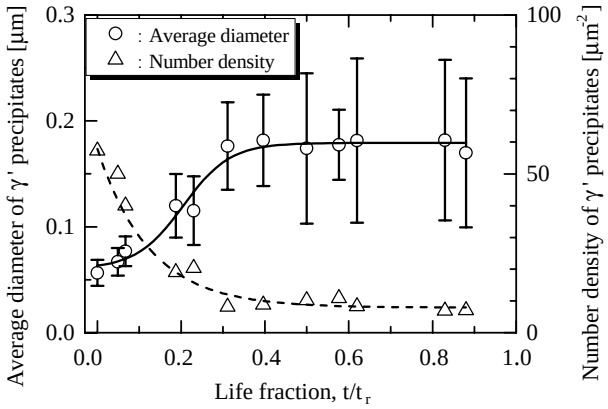

Fig. 16. Change of the average diameter and number density of γ' phase as the creep progress in *Continuous test* (140 MPa, 1073 K).

ultrasonic stress. Note that Eq. (6) is not applied to all the dislocations but is aimed at dislocations oscillated by a low stress wave with ultrasonics. We define these dislocations as *movable* dislocations, which result in the ultrasonic attenuation. Dislocations piling up grain boundaries or γ' precipitates can not vibrate and fail to contribute to the change of α. It was clear that the attenuation coefficient with EMAR enabled to detect the evolution of the dislocation structure as fatigue progresses of pure copper and a low carbon steel (Ogi et al., 2000; Hirao et al., 2000; Ohtani et al., 2001c) and creep progress of a stainless steel and 2.25%Cr-1%Mo steel(Ohtani et al., 2001a,b). One expects that change of the attenuation reflects the evolution of the dislocation structure in Waspaloy during the creep.

We, then, observed the microstructure by TEM. Fig. 17 shows the TEM micrographs. Fig. 17 (a) shows the dislocation structure before the creep, $t/t_r = 0$ and Fig. 17(b)–(d), at $t/t_r = 0.23$, 0.5 and 0.88. Dislocation density is very low before the creep and the average dislocation length is around 0.5–0.6 μm. Fine γ'-precipitates less than 0.05 μm diameter uniformly distributed and the distance between γ'-precipitates is around 0.05 μm. Fig. 17(b) shows the microstructure at $t/t_r = 0.23$, when α increases gradually (Fig. 12). Many dislocations pinned by γ'-precipitates are observed. In Fig. 17(c), many tangled dislocations near γ' precipitates are observed, when α decreases rapidly. In Fig. 17(d), tangled dislocations entirely cover the whole area.

From these TEM and SEM micrographs in Figs. 15–17 and some quantitative results (Barrett et al., 1966; Hasegawa et al., 1972; Orlova and Cadek, 1973; Sikka et al., 1975; Takeuchi and Argon, 1976; Okazaki et al., 1992; Blum, 1993; Ohtani et al., 2001a,b), the evolution of the microstructure and change of the attenuation coefficient as the creep progress shown in Fig. 13 is described below in three stages. In Fig. 12, the creep strain rate always increases. Then, the creep strain rate $\dot{\varepsilon}$ is described as follows (Cadek, 1988; Nabarro and de Villier, 1995):

$$\dot{\varepsilon} \sim A_3 \sigma^m n(\varepsilon) v(\varepsilon), \tag{7}$$

where σ is a stress, $n(\varepsilon)$ the dislocation density (contributes to deformation at the creep strain of ε), $v(\varepsilon)$ dislocation rate, and A_3 and m constants.

The whole phenomena can be explained as follows. Before the creep, dislocation density is very low and fine γ'-precipitates distribute uniformly.

(1) Stage I ($0 < t/t_r < 0.3$): From the start to about 30% of the life time, the increase in creep strain is expected to see the development of dislocation (multiplication, slip) (Fig. 17(b)) and the increase in dislocation density (Eq. (7)). Besides, rapid coarsening and condensation of γ'-precipitates (Fig. 16) are

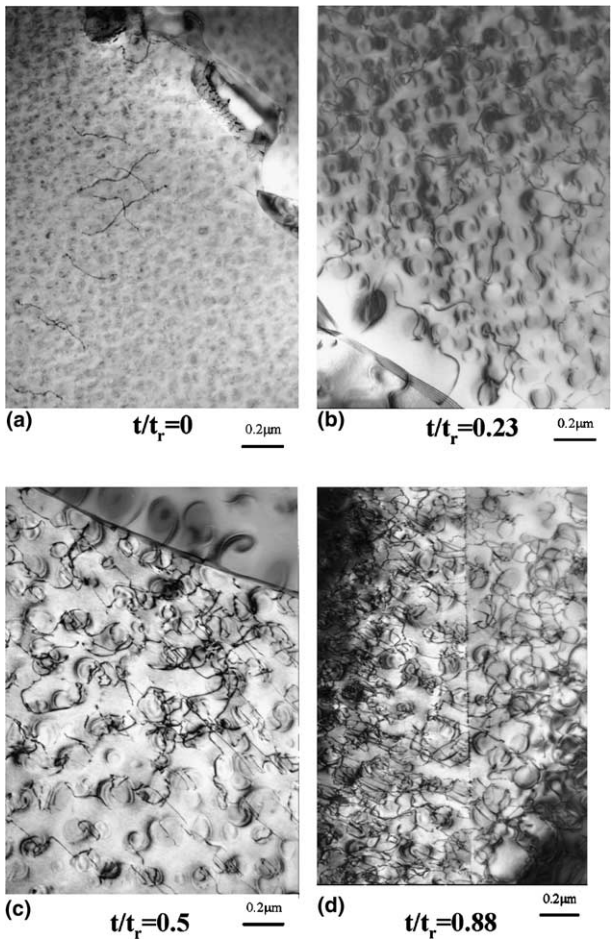

Fig. 17. Transmission electron micrographs of crept specimens at $t/t_r = 0$, 0.23, 0.5 and 0.88 in *Continuous test* (140 MPa, 1073 K).

expected to see rapid increases in size of γ' precipitates and distance between them. Furthermore, the coarsening and condensation make the distance of pinned dislocations and their movability increase. As a result, the increases of Λ and L lead to the increase of α.

(2) Stage II ($0.3 \leqslant t/t_r < 0.5$): For the period of 30–50% the lifetime, total dislocation density continuously increases with increase in creep strain. The rate of coarsening and condensation seems to become slow as shown in Fig. 16. Then the dislocations piling up on the precipitates increase (Fig. 17(c)). As a result, the following behavior is brought about; the distance between the dislocations becomes narrow and then the stress caused by the interaction among dislocations obstructs dislocation movements. Therefore, drastic decreases in Λ and L lead to a drastic reduction in α and then α shows the peak. At the peak, creep strain is around 2% and $t/t_r = 0.3$.

(3) Stage III ($0.5 \leqslant t/t_r$): Over 50% lifetime, the coarsening and condensation are saturated as shown in Fig. 16. By the further deformation, tangling and piling of dislocations make progress still more (Fig. 17(d)). *Movable* dislocation exists few. α remains unchanged or decreases slightly.

We consider that the peak of α around 30% of the lifetime is correspondence to the initiation of tangling by multiplying dislocations and γ'-precipitates. At that time, the rate of the coarsening and condensation of γ '-precipitates begins to slow. The attenuation peak was observed in the creep progresses on an austenitic stainless steel (JIS-SUS304) and 2.25%Cr–1%Mo steel (Ohtani et al., 2001a,b). These show the universality of the EMAR method. In addition, the method is capable of capturing the microstructure evolution, dislocation mobility and the coarsening and condensation of γ'-precipitates, as the creep progress.

5. Conclusion

The high sensitivity and contactless aspects of EMAR enabled the precious measurement of the resonant frequency and ultrasonic coefficient during creep progressing of nickel-based superalloy, Waspaloy. Shear-wave attenuation always showed a peak at 35–40% of life time, being independent of the applied stress. This observation was first made possible with the EMAR method. We interpreted this phenomena in terms of dislocation mobility and coarsening of γ'-precipitates, which is supported by the SEM and TEM observations. The attenuation peak exhibits a characteristic event in which the multiplied dislocations start tangling to γ'-precipitates and dislocations and the coarsening and condensation of γ'-precipitates begin to slow. The relationship between attenuation change and the microstructure evolution can be explained with the string's model. The attenuation coefficient has a good correlation with the life fraction, rather than the creep strain and time. EMAR has a potential to assess the damage advance and to predict the remaining creep life of metals.

References

Birring, A.S., Alcazer, D.G., Hanley, J.J., Gehl, S., 1989. Detection of creep damage by ultrasonics, In: Review of Progress in Quantitative Non-destructive Evaluation, **8B**. Thompson, D.O., Chimenti, D.E., editors, Plenum Press, New York, 1833–1840.

Barrett, C.R., Nix, W.D., Sherby, O.D., 1966. The influence of strain and grain size on the creep substructure of Fe–Si. Transaction of American Society for Metals 59, 3–15.

Bergheau, J.M., Devaux, J., Mottet, G., Gilles, P., 2004. Prediction of creep rupture of pressure vessels. Journal of Pressure Vessel Technology 126, 163–168.

Bhandari, S., Feral, X., Bergheau, J.M., Mottet, G., Dupas, P., Nicholas, L., 2000. Creep-damage analysis: comparison between coupled and uncoupled methods. Journal of Pressure Vessel Technology 122, 408–412.

Blum, W., 1993. in: R.W. Cahn, P. Haasen, E.J. Kramer (eds.), Materials Science and Technology. VCH Verlagsgesellschaft mbH, 359-405.

Cadek, J., 1988. Creep in Metallic Materials. Elservier, Amsterdam, 95–114.

Clark, A.V., Fortunko, C.M., Lozev, M.G., Schaps, S.R., Renken, M.C., 1992. Determination of sheet steel formability using electromagnetic-acoustic transducers. Research in Nondestructive Evaluation 4, 165–182.

Delong, R.T., 1987. Standard Practice for Prediction and Evaluation of Field Metallographic Replicas, E12-87, American Society for Testing and Materials, Philadelphia.

Dooley, R.B., Viswanathan, R., editors, 1987. Life extension and assessment of fossil power plants. In: Proceedings of Conference in Washington, June 1986, ERPICS5208, Electric Power Research Institute, Palo Alto, CA.

Dunn, K.M., Scheibel, J.R., Schwartz, F., 1985, Monitoring for Life Extensions, TIS-PSG-85-001, Combustion Engineering, Windsor, CT.

Ellis, F.V., Loomi, R.W., Tordonato, S., 1987. Life extension: the CE approach to the analysis of thick walled components. In: Dooley, R.B., Viswanathan (Eds.), Life Extension and Assessment of Fossil Power Plants. Reports CS 5208, Electric Power Research Institute, Palo Alto, CA, 335–350.

Furtonko, C.M., Petersen, G.L., Chick, B.B., Renken, M.C., Peris, A.L., 1992. Absolute measurement of elastic-wave phase and group velocities in lossy materials. Review of Scientific Instruments 63, 3477–3486.

Goebbels, K., 1980. Structure Analysis by Scattered Ultrasonic Radiation. Res. Tech. in NDT. Academic Press, London, 4, 87–157.

Granato, A., Lücke, K., 1956. Theory of mechanical damping due to dislocation. Journal of Applied Physics 27, 583–593.

Hasegawa, T., Ikeuch, Y., Karashima, S., 1972. Internal stress and dislocation structure during sigmoidal transient creep of a copper-16 at.% aluminum alloy. Metal Science Journal 6, 78–82.

Hirao, M., Morishita, T., Fukuoka, H., 1990. Ultrasonic velocity change with creep damage in copper. Metallargical Transactions A 21A, 1725–1732.

Hirao, M., Ogi, H., Fukuoka, H., 1993. Resonance EMAT system for acoustoelastic stress measurement in sheet metals. Review of Scientific Instruments 64, 3198–3205.

Hirao, M., Ogi, H., 1997. Electromagnetic acoustic resonance and materials characterization. Ultrasonics 35, 413–421.

Hirao, M., Ogi, H., Suzuki, N., Ohtani, T., 2000. Ultrasonic attenuation peak during fatigue of polycrystalline copper. Acta Materialia 48, 517–524.

Kachanov, L.M.., 1958. Time of the rupture progress under creep conditions. Izv. Akad. Nauk. SSSR, Otd. Tekh. Nauk. Topl. 8, 26–31.

Jaske, C.E., Simonen, F.A., Roach, D.B., 1983. Predict reformer furnace tube life. Hydrocarbon Processing 62, 63–68.

Johnson, W., Norton, S., Bendec, F., Pless, R., 1992. Ultrasonic spectroscopy of metallic sphere using electromagnetic-acoustic transduction. Journal of Acoustical Society of America 91, 2637–2642.

Johnson, W., Auld, B.A., Alers, G.A., 1994. Application of Resonant modes of Cylinders to Case Depth Measurement, in Review of QNDE, 13, pp. 1603–1610.

Kishimoto, S., Shinya, N., Matsumoto, S., Fukuhara, H., 1988. Evaluation of creep cavity by measurement of ultrasonic velocity. In: Proceeding of 26th symposium on Strength of Materials at High Temperatures. The Society of Materials Science, Tokyo, Japan, December 1988, pp. 11–15 (in Japanese).

Maruyama, K., Harada, C., Oikawa, H., 1985. A strain-time equation applicable up to tertiary creep stage. Journal of Society of Materials Science, Japan 34, 1289–1295.

Maruyama, K., Oikawa, H., 1987. An extrapolation procedure of creep data for S_t determination: with special reference to Cr–Mo–V steel, Transaction of American Society of Mechanical Engineerings. Journal of Pressure and Vessel Technology 109, 142–148.

Miller, A.K., 1987. Unified Constitutive Equations for Creep and Plasticity. Elservier Applied Science, London and New York, 1–301.

Morishita, T., Hirao, M., 1997. Creep damage modeling based on ultrasonic velocities in copper. International Journal of Solids and Structure 34, 1169–1175.

Nabarro, F.R.N., de Villier, H.L., 1995. The Physics of Creep: Creep and Creep-resistant Alloys. Taylor & Francis Publisher, pp. 15–46.

Nakashiro, M., Yoneyama, H., and Ohtomo, A., 1987. Assessment for Creep damage of boiler tube by newly researched ultrasonic technique. International Conference on Advances in Material Technology for Fossil Power Plants, ASME International, Metals Park, Ohio, pp. 351–358.

Neubauer, B., Wedel, U., 1983. Restlife estimation of creep components by means of replica. In: Woodford, D.A., Whitehead, J.R. (Eds.), Advances in Life Prediction Methods. American Society of Mechanical Engineerings, New York, pp. 307–314.

Ledbetter, H.M., Fields, R.J., Datta, S.K., 1987. Creep cavities in copper: an ultrasonic velocity and composite modeling study. Acta Metallica 35, 2393–2398.

Ogi, H., Hirao, M., Hamaguchi, T., 2000. Ultrasonic attenuation peak in steel and aluminum alloy during rotating bending fatigue. Metallurgical and Materials Transactions A 31A, 1121–1128.

Ogi, H., Hirao, M., Honda, T., Fukuoka, H., 1995. Absolute Measurement of Ultrasonic Attenuation by Electromagnetic Acoustic Resonance. in: Review of Progress in Quantitative Non-destructive Evaluation, 14, pp. 1601–1608.

Ohtani, T., Ogi, H., Hirao, M., 2001a. Change of ultrasonic attenuation and microstructure evolution in crept stainless steel. Transaction of Japanese Society of Mechanical Engineers Series A 67 (655), 454–461.

Ohtani, T., Ogi, H., Hirao, M., 2001b. Change of ultrasonic attenuation and microstructure evolution in crept 2.25–1%Mo steels. Journal of Society of Materials Science, Japan 51, 195–201.

Ohtani, T., Ogi, H., Hirao, M., 2001c. Ultrasonic attenuation monitoring of fatigue damage in low carbon steels with electromagnetic acoustic resonance (EMAR). Journal of Alloys and Compounds 310, 440–444.

Okazaki, M., Hashimoto, M., Sada, T., 1992. An approach on nondestructive detection of creep damage in SUS316 steel through ultrasonic attenuation properties. Journal of Society of Materials Science Japan 41 (47), 1729–1735.

Orlova, A., Cadek, J., 1973. Some substructure aspects of high-temperature creep in metals. Philosophical Magazine 28, 891–899.

Papadakis, E.P., 1984. Absolute measurement of ultrasonic attenuation using damped nondestructive testing transducers. Journal of Testing and Evaluation 12, 273–279.

Rabotnov, Y.N., 1969. Creep Problem in Structural Members, North Holland.

Rosen, G.I., Dirnfeld, S.F., Bamberger, M., Rosen, A., Prinz, B., 1993. Creep investigation of commercial and Improved Nickel-based Wrought Supperalloy. Materials Science and Engineering A 172, 15–21.

Sikka, V.L., Nahm, H., Moteff, J., 1975. Some aspects of sub-boundary and mobile dislocations during high temperature creep of AISI 316 and 304 stainless steels. Materials Science and Engineering 20, 55–62.

Takeuchi, S., Argon, A.S., 1976. Review steady-state creep of single-phase crystalline matter at high temperature. Journal of Materials Science 11, 1542–1566.

Truell, R., Elbaum, C., Chick, B., 1969. Ultrasonic Methods in Solid State Physics. Academic Press, New York, pp. 159–249.
Viswanathan, R., 1989. In: Damage Mechanism and Life Assessment of High Temperature Components. ASME International, Metals Park, Ohio, pp. 59–110, and 225–227.
Willems, H., Bendick, W., Weber, H., 1987. Nondestructive evaluation of creep damage in service exposed 14 MoV 63 steel. In: Brussiere, J.F., Ruud, Monchalin J., Green, R.E. Jr. (Eds.), Nondestructive Characterization of Materials II. Plenum Press, New York, pp. 451–459.